

# An XSPEC model to explore spectral features from black-hole sources — II.

## The relativistic iron line in the lamp-post geometry

Michal Dovčiak,<sup>1,a</sup> Jiří Svoboda,<sup>1</sup> René W. Goosmann,<sup>2</sup>  
Vladimír Karas,<sup>1</sup> Giorgio Matt<sup>3</sup> and Vjačeslav Sochora<sup>1</sup>

<sup>1</sup>Astronomical Institute, Academy of Sciences of the Czech Republic,  
Boční II 1401, CZ-141 00 Prague, Czech Republic

<sup>2</sup>Observatoire Astronomique de Strasbourg,  
11 rue de l'Université, F-67000 Strasbourg, France

<sup>3</sup>Dipartimento di Matematica e Fisica, Università degli Studi “Roma Tre”,  
Via della Vasca Navale 84, I-00146 Roma, Italy

<sup>a</sup>dovciak@asu.cas.cz

### ABSTRACT

In X-ray spectra of several active galactic nuclei and Galactic black hole binaries a broad relativistically smeared iron line is observed. This feature arises by fluorescence when the accretion disc is illuminated by hot corona above it. Due to central location of the corona the illumination and thus also the line emission decrease with radius. It was reported in the literature that this decrease is very steep in some of the sources, suggesting a highly compact corona.

We revisit the lamp-post setup in which the corona is positioned on the axis above the rotating black hole and investigate to what extent the steep emissivity can be explained by this scenario. We show the contributions of the relativistic effects to the disc illumination by the primary source — energy shift, light bending and aberration. The lamp-post radial illumination pattern is compared to the widely used radial broken power-law emissivity profile. We find that very steep emissivities require the primary illuminating source to be positioned very near the black hole horizon and/or the spectral power-law index of the primary emission to be very high. The broken power-law approximation of the illumination can be safely used when the primary source is located at larger heights. However, for low heights the lamp-post illumination considerably differs from this approximation.

We also show the variations of the iron line local flux over the disc due to the flux dependence on incident and emission angles. The former depends mainly on the height of the primary source while the latter depends on the inclination angle of the observer. Thus the strength of the line varies substantially across the disc. This effect may contribute to the observed steeper emissivity.<sup>1</sup>

<sup>1</sup> This paper summarises the work done for the workshop *Ragtime12* held in 2010.

**Keywords:** accretion, accretion discs – black hole physics – line: formation – line: profiles – relativistic processes – X-rays: galaxies – X-rays: binaries

## 1 INTRODUCTION

The broad iron line in the X-ray spectra of active galactic nuclei (AGN) and Galactic X-ray binaries has been studied by various authors for more than two decades. The first mention of the relativistic broadening of spectral lines due to high orbital velocities of the accretion disc, where the iron  $K\alpha$  line arise by fluorescence, dates as far as 1989 when Fabian et al. studied the X-ray spectrum of Cygnus X-1 observed by EXOSAT in 1983. Since then the relativistically broadened line was discovered in systems with diverse masses: in AGN with central supermassive black holes (e.g. Risaliti et al., 2013), in X-ray binaries with the black hole of several solar masses (e.g. Miller et al., 2013) and even in systems with a neutron star (e.g. Cackett and Miller, 2013). Although the broad lines seem very well established, one should mention that there exist an alternative explanation of the phenomena — partially covering scenario proposed by Miller and Turner (2013). However, recent X-ray reverberation studies of AGN support the reflection scenario, see e.g. Fabian et al. (2013).

The shape of the observed line is determined by several factors: by the geometry of the illuminating and reflecting region, by the physical properties of the re-processing matter and by the properties of the central gravitating body. The shaping of line, mainly its broadening, by the black-hole gravitation acting on photons emitted in the inner accretion disc is used to measure the spin of the black hole. Actually, high energy redshift due to large gravity near the centre is completely responsible for the extreme width of the line. The other components can modify the overall line profile, yet, they are not able to change the width of the line by themselves. Still their contribution may be important in determining the spin value. This is caused by the particular shape of the relativistically broadened line — the line flux gradually decreases with the decreasing energy, thus the lower edge of the line is not easily pinpointed, its determination depends on how strong the line's red wing is and the contribution of the mentioned components may be important.

One of the inevitable components, that makes the formation of the fluorescent line possible, is the illuminating corona. Its geometry will affect the illumination of the disc and consequently also the emission of the line from different parts of the disc. This will eventually alter the overall line profile. Usually the corona is supposed to be either extended (e.g. Wilkins and Fabian, 2012) over large area above the disc or concentrated in a compact region (e.g. Fabian et al., 2011). In the first case the illumination of the disc is often assumed to be a broken power-law function of the radius, with more intensive illumination and resulting higher line emission in the inner parts of the disc. Sometimes the observed radial power-law near the black hole is quite steep (Wilkins and Fabian, 2011) and it was suggested (Svoboda et al., 2012) that it could be caused by the second possible scenario, i.e. sort of

a lamp-post configuration, where the compact patch of the corona located above the black hole illuminates the accretion disc, sometimes referred to as an aborted jet scenario (Ghisellini et al., 2004) or a light bending model (Miniutti and Fabian, 2004). In this geometry, the illumination of the disc is due to a compact primary source and photon trajectories close to the centre are bent by strong gravity of the black hole. Consequently, the radial profile of the line emission takes a particular form that depends on the height of the lamp-post.

In this paper we compare the two radial profiles of the line emission — the broken power-law dependence and illumination in the lamp-post scenario. We concentrate mainly on the question if the observed steep radial decrease of the emissivity could be interpreted in terms of the lamp-post geometry. To this purpose we at first assume very simple local physics of the emission, particularly, the emission does not depend on incident and emission angles, and the flux in line is isotropic and proportional to the incident flux. Then, we also apply the emission directionality given by the numerical modelling of radiative transfer (using Monte Carlo multi-scattering code NOAR, see Dumont et al., 2000).

## 2 RELATIVISTIC LAMP-POST GEOMETRY

The lamp-post geometry has been introduced to describe the observed emission from X-ray irradiated accretion discs by Matt et al. (1991) and Martocchia and Matt (1996). The model consists of an X-ray source (‘lamp’) producing the primary irradiation and representing an optically thin corona that is thought to extend above the optically thick medium of a standard accretion disc (Frank et al., 2002). This scheme has proved to be very popular in the context of accreting supermassive black holes in cores of AGN (Peterson, 1997). Location of the primary source on the black hole axis can be imagined, e.g., as a site of action where jets are initially accelerated (Biretta et al., 2002) or where the shocks in an aborted jet collide (Ghisellini et al., 2004). A down-scaled version of the model has been also invoked to describe microquasars (Mirabel and Rodríguez, 1998).

The lamp-post geometry (on or off-axis) has already been studied in various context by several authors – AGN variability was studied by (Miniutti and Fabian, 2004) and Niedźwiecki and Miyakawa (2010), the polarisation properties were investigated by Dovčiak et al. (2011) and the X-ray reverberation mapping by Emmanoulopoulos et al. (2014) and Cackett et al. (2014). Recently, Dauser et al. (2013) has studied disc reflection due to illumination by a jet, i.e. radially extended region moving along the axis.

Despite the fact that realistic corona must be a very complex, inhomogeneous and turbulent medium, the lamp-post model captures the main components of a typical AGN spectrum, and it allows us to search for the parameter values. In particular, the slope of the primary power-law continuum, and the skewed and redshifted profile of the broad iron line around 6–7 keV that has been interpreted in terms of relativistically smeared reflection spectrum.

It has been shown (Wilms et al., 2001) that a steep emissivity profile of  $\simeq 4.3$ -5.0 of the iron-line and reflection features are required in XMM-Newton observation of MCG-6-30-15. This has been interpreted in terms of highly central concentration of the irradiating flux, in a much more compact nuclear region than predicted by pure accretion disc models. Similarly steep emissivity profile has been reported in 1H0707-495 (Fabian et al., 2009) and IRAS13224-3809 (Ponti et al., 2009). In order to explain the unusually steep spectrum, Wilms et al. (2001) invoke some additional X-ray source that is presumably associated with the extraction of the black hole spin energy, perhaps via some kind of magnetic coupling (Blandford and Znajek, 1977).

The main aim of the present investigation is to verify whether the relativistic effects can produce the steep emissivity required by the mentioned observations. To this end we consider Kerr metric for the gravitation of a rotating black hole, and we allow for both prograde and retrograde rotation of the accretion disc with respect to the black hole spin.

A complex interplay of the energy shifts, aberration, boosting and light-bending effects acts on the primary as well as reflection components of the X-ray spectrum, especially when the source of irradiation is placed at a small height near above the horizon and if the black hole rotates rapidly, so that the inner edge of the disc is at a small radius. As a result of this interplay, it is not obvious at all whether the resulting emissivity comes out significantly steeper in comparison to the non-relativistic limit of an irradiated standard disc.

To study the radial emissivity we first turn our attention to the reflected line component. We assume the line flux to be proportional to the incident flux and the photons will be emitted isotropically in local frame co-rotating with the Keplerian disc, no matter what the incident and emission angles are. In this way we are going to study the effect of the relativistic lamp-post geometry only, separating it from the effects due to the dependence of the local physics on geometry of the incident and emission light rays.

In this approach the local line emission in the disc is proportional to the normalization of the power-law incident flux. We assume the primary emission to be isotropic in local frame and that it is a power law with the photon index  $\Gamma$ , i.e.  $f_i(E_i) = N_i E_i^{-\Gamma}$ . Then the incident flux,  $f_i$ , is a power law with the same photon index but with a different normalization

$$f_i(E_i) = N_i(r) N_i E_i^{-\Gamma} . \quad (1)$$

Here, the normalization  $N_i(r)$  is given by the curved geometry of the light rays and relativistic shift of the energy. It can be expressed in the following way (see e.g. Dovčiak, 2004)

$$N_i(r) = g_i^\Gamma \frac{d\Omega_i}{dS_i} = \frac{g_i^{\Gamma-1}}{U_i^t} \frac{d\Omega_i}{dS} . \quad (2)$$

The primary photons emitted by the lamp-post into the local solid angle  $d\Omega_i$  fall down onto the disc area measured in the frame co-moving with the disc  $dS_i =$



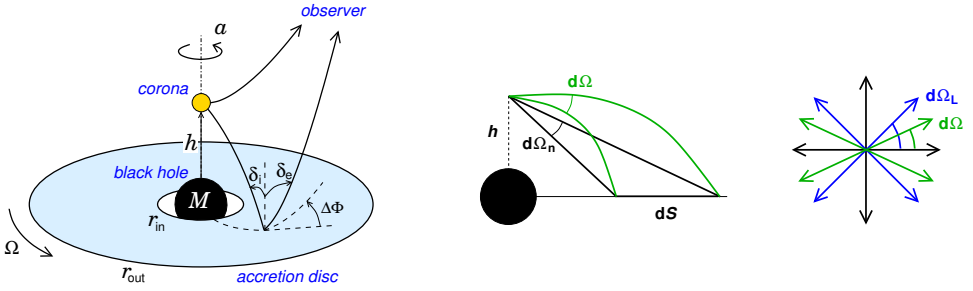


**Figure 1.** *Left:* The sketch of the lamp-post geometry. *Middle:* Due to the light bending the photons illuminating the same area of the disc are emitted by the primary source into different solid angles in the relativistic and the Newtonian cases. *Right:* The photons emitted isotropically in the rest frame of the primary source are beamed perpendicularly to the rotation axis because of the strong gravity near the black hole.

$p_{i\mu}U^\mu dS = g_i U_1^t dS$ . These photons are shifted to the incident energy  $E_i$  from the emission energy  $E_1$  by the energy shift  $g_i = E_i/E_1 = p_{i\mu}U^\mu/p_{1\mu}U_1^\mu$  which is responsible for the factor of  $g_i^\Gamma$  in the above equation. We have denoted the four-momentum of the incident photons by  $p_i^\mu$ , the four-velocity of the static lamp-post by  $U_1^\mu = (U_1^t, 0, 0, 0)$  and the four-velocity of the disc by  $U^\mu$ . We assume the disc to be Keplerian above the marginally stable orbit and freely falling below it with the constant energy and momentum that the matter had at this orbit. The area element  $dS = r dr d\varphi$  is evaluated in Boyer-Lindquist coordinates.

The normalization of the incident flux,  $N_i$ , is a function of radius, and thus it determines the radial emission profile of the line flux. We can separate this function into several components

$$N_i(r) = \frac{1}{r} \frac{d\mu_n}{dr} \times \frac{g_i^{\Gamma-1}}{U_1^t} \times \frac{d\mu}{d\mu_n} \times \frac{d\mu_l}{d\mu}. \quad (3)$$

The first component is chosen in such a way that it represents exactly the Newtonian value of  $N_i(r)$

$$N_i^n(r) \equiv \frac{d\Omega_n}{dS} = \frac{1}{r} \frac{d\mu_n}{dr} = \frac{h}{(r^2 + h^2)^{3/2}}. \quad (4)$$

In the above, we have introduced the Newtonian angle of emission,  $\theta_n$ , as the angle under which the primary photon has to be emitted from the lamp-post at height  $h$  in the Newtonian non-curved space so that it falls down onto the disc at the radius  $r$  and  $\mu_n \equiv \cos \theta_n$ .

The second component,  $g_i(r)^{\Gamma-1}/U_1^t$ , is connected with the energy shift of the incident photons and it should be emphasized that it depends on the primary flux via the photon index  $\Gamma$ . For Keplerian discs in the Kerr space-time it can be

expressed above the marginally stable orbit as

$$N_i^s(r) = \left( \frac{r^2 + a\sqrt{r}}{r\sqrt{r^2 - 3r + 2a\sqrt{r}}} \right)^{\Gamma-1} \left( 1 - \frac{2h}{h^2 + a^2} \right)^{\frac{\Gamma}{2}}. \quad (5)$$

The third component,

$$N_i^b(r) \equiv \frac{d\Omega}{d\Omega_n} = \frac{d\mu}{d\mu_n} = \frac{\sin\theta}{\sin\theta_n} \frac{d\theta}{d\theta_n}, \quad (6)$$

represents the effects of the light bending in the curved space-time. It compares the solid angle  $d\Omega$  in the Boyer-Lindquist coordinates with the Newtonian value, defined above, into which primary photons have to be emitted to illuminate the disc area  $dS$  at the disc radius  $r$ .

The fourth component represents the “gravitational aberration”. Due to the fact that the local observers on the axis measure the distances differently along the axis and perpendicular to it, the local isotropic emission will be beamed in Boyer-Lindquist coordinates in the direction perpendicular to the axis. We can express it by comparing the solid angle in local frame of the lamp-post with the solid angle in Boyer-Lindquist coordinates

$$N_i^a(r) = \frac{d\Omega_l}{d\Omega} = \frac{h}{\sqrt{\Delta_h}} \left[ 1 + \left( \frac{\Delta_h}{h^2} - 1 \right) \cos^2\theta_l \right]^{3/2}, \quad (7)$$

where  $\Delta_h \equiv h^2 - 2h + a^2$  and the photon’s local emission angle  $\theta_l$  is a function of the radius  $r$  at which such a photon strikes the disc. One can see that the solid angle  $d\Omega$  is amplified by the factor  $h^2/\Delta_h > 1$  along the axis ( $\theta_l = 0^\circ$  or  $\theta_l = 180^\circ$ ) and it is diminished by the factor  $\sqrt{\Delta_h}/h < 1$  in the direction perpendicular to the axis ( $\theta_l = 90^\circ$ ).

On the top panels of Fig. 2 we show the radial profile of the function  $N_i(r)$  and its components for extremely rotating black hole and for several heights of the primary source. In Newtonian case the illumination of the disc is flat below the lamp-post and decreases with the radius with the third power far from the centre. The energy shift component is higher than unity for the radius lower than the height of the lamp-post (however, due to the Doppler shift and black hole spin the transition radius is somewhat shifted) and it is lower than unity above this radius. It is due to the fact that in the first case the photon falls closer to the black hole, gaining the energy, whereas in the second case it climbs out of the gravitational potential well, losing its energy. As a result, the shift gains very high values for small radii close to the horizon and quite low values far from the black hole if the height of the primary source is low.

The effect of light bending is stronger closer to the black hole. Thus the photon trajectory that is nearer to the black hole is more curved, the difference in bending of two close trajectories gets smaller farther away from the centre. This results in light bending component  $N_i^b(r)$  to be a decreasing function of radius.

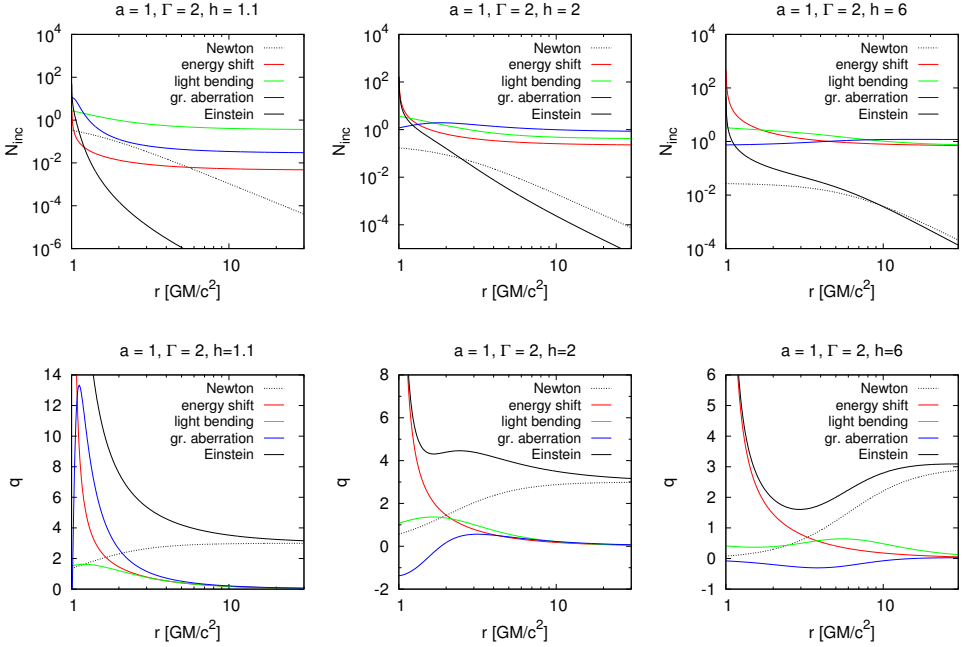


**Figure 2.** The radial profile of the incident flux  $N_i(r)$  (top) and its radial power-law index  $q(r)$  (bottom) in the relativistic lamp-post geometry with the illuminating primary source at heights  $h = 1.1, 2$  and  $6 GM/c^2$  (from left to right). The primary flux is a power law with the index  $\Gamma = 2$  and the Kerr black hole rotates extremely with the spin  $a = J/M = 1 GM/c$ . The contributions from the Newtonian, energy shift, light bending and gravitational aberration parts are shown. The solid black line (Einstein) depicts the overall incident flux and its radial power-law index.

Due to the fact that the gravitational aberration decreases the solid angle, which photons are emitted into, the most in the direction perpendicular to the axis, the incident flux will be amplified for those radii where the photons emitted in this direction strike the disc. That is why the component  $N_i^a(r)$  first increases with the radius and then decreases. The maximum moves farther away from the black hole for higher lamp-post. For very low heights of the primary source, the photon trajectories emanating perpendicularly to the axis are bend so much that they do not strike the disc, rather they fall onto the horizon. In that case this component of the incident flux decreases with the radius.

To compare the relativistic lamp-post illumination with the broken power law one, we define the radial power-law index for the lamp-post geometry as the slope of the radial profile of  $N_i(r)$  in the log-log graph (i.e. slope of the graphs on top panels in Fig. 2). The definition reads

$$q(r) \equiv \frac{d \log N_i(r)}{d \log r} = -r \frac{d}{dr} \ln N_i(r) . \quad (8)$$

The radial power-law index defined in this way clearly depends on the radius. The four components of the incident flux that has to be multiplied to give the overall illumination translate into four components of the power-law index  $q(r)$  that have to be added to give the overall relativistic radial power-law index. We show all four components of the index on bottom panels in Fig. 2.

The index  $q(r)$  for large radius is given by the Newtonian value,  $q(r \rightarrow \infty) = 3$ . For very low radii, close to the horizon, the energy shift component dictates the behaviour of the  $q(r)$ . Its influence extend farther for higher primary spectral power-law index. For very low heights, heights near above the black hole horizon, the component due to gravitational aberration adds also quite significantly to the index for low radius. For low lamp-post heights ( $h \lesssim 6 GM/c^2$ ), the light bending and gravitational aberration component may create local maxima in the radial power-law index, depending on the black hole spin and primary spectral power-law index  $\Gamma$ . More examples of the behaviour of the radial power-law index  $q(r)$  for different parameter values are shown in Fig. A2. Note, that if the line emission were proportional to the incident flux also below the marginally stable orbit (dotted lines in Fig. A2), the index  $q(r)$  for lower absolute value of the black hole spin, i.e. larger radius of the event horizon, would be larger. This is due to the energy shift component of the  $q(r)$ , which gains large values also at higher radii.

From Figs. 2 and A2 it is evident that the relativistic lamp-post illumination is very different from the broken power law, which would be represented by two constant values in these figures. For comparison, we show the relativistic lamp-post emission together with a broken power law in Fig. A1. The graphs in this figure are renormalized in such a way that they do not intersect each other, here, we are interested in their shape only. The broken-power-law graphs (depicted by red) have Newtonian value of the index,  $q_{\text{out}} = 3$ , above the break radius,  $r_b$ . The break radius and index  $q$  below it were chosen by eye so that they approximately represent the relativistic lamp-post flux. We show their values in Tables A1–A4. One can see that the broken power law is close enough only in some radial regions whereas it fails for small radii near the horizon and region around the break radius. Although the difference between the two is large in these regions (note, that the graphs are in logarithmic scale), one still cannot jump to the conclusion that the broken power-law approximation would fail in fitting the spectra originated in the relativistic lamp-post geometry. The energy of the photons coming to the observer from regions close to the horizon is strongly shifted to very low values and the troublesome region near the break radius may be small enough with respect to the whole disc to change the overall spectrum. Thus the spectra for the broken power-law emissivity and for relativistic lamp-post geometry might still be similar sufficiently.

From graphs in Fig. A1 one can see that the illumination profile would actually be much better approximated with a power-law with two breaks instead of one, especially for higher locations of the primary source. Comparisons between simple power-law and once or twice broken power-law are investigated by Wilkins and Fabian (2011).

### 3 THE DIRECTIONALITY OF THE LOCAL FLUX

The flux emitted by the primary source illuminates the disc and the incident photons are then re-processed in the orbiting material. They scatter on electrons, are absorbed by ions or neutral atoms or they can be created by the fluorescence when electrons in ions or neutral atoms change their state. Fluorescent spectral lines, line edges and Compton hump are typical features of such reflected X-ray spectra (Ross and Fabian, 2005; García et al., 2013). The most prominent spectral line in this energy band is that of iron (Fe K $\alpha$  line doublet for neutral iron is at 6.4 keV) due to its large abundance and high fluorescence yield. The flux emitted locally in this line depends on number of absorbed photons that create the vacancies and fluorescent yield which characterises how fast these vacancies fill. If we assume that there is always enough photons that induce the fluorescence then the flux in the line is mainly dependent on the absorption. A vacancy at the K level of a neutral iron line is created when a photon with the energy above the iron K edge (at approx. 7.1 keV) is absorbed. The efficiency of the absorption quickly decreases with the energy, thus only photons up to a few keV above this edge are absorbed. This is due to the fact that the K-absorption cross-section of a photon with energy  $E$  above the K-absorption edge at 7.1 keV (measured in the local disc frame) decreases approximately as (Verner et al., 1993)  $1.9 (E/7.1 \text{ keV})^{-3.1} - 0.9 (E/7.1 \text{ keV})^{-4.1}$  and thus levels off to 1% of its initial value already at 37.4 keV. Since the primary spectrum assumed in our model extends to much higher energies, the flux in the line is simply proportional to the normalisation of the incident power-law spectrum. We generally assume that both cut-off energies of the primary spectrum lie outside the energy band where absorption occurs. We give two examples for extremely rotating Kerr black hole to show how well this assumption is fulfilled:

(1) The lower energy cut-off is shifted to higher energy when the primary source is very high above the disc. Then the incident photons gain the highest energy if they fall close to the horizon. For the lamp at height  $h = 100 \text{ GM}/c^2$  and incident radius at  $r_i = 1.035 \text{ GM}/c^2$  the photon energy shift is  $g_i = 67$ . Thus the lower energy cut-off at 0.1 keV would be shifted to 6.7 keV which is still below the Fe K edge. Note, that the emission below this region will have very low contribution to the overall spectral shape of the observed broadened line both due to small emission area and due to small value of the transfer function (that amplifies local flux when transferred to the observer at infinity),  $G < 0.1$  for inclination  $\theta_o = 70^\circ$  (and smaller for lower inclinations). The contribution from this region will be shifted by the factor  $g < 0.1$ , thus to energy  $E < 0.64 \text{ keV}$ .

(2) The high energy cut-off is shifted to lower energy when the primary source is very low above the black hole horizon. Then the incident photons lose the energy when they have to climb out of deep potential well, thus they lose more if they fall to the disc far away from the horizon. For the lamp at height  $h = 1.3 \text{ GM}/c^2$  and incident radius at  $r_i = 1000 \text{ GM}/c^2$  the photon energy shift is  $g_i = 0.186$ . Thus the higher energy cut-off at 200 keV would be shifted to 37.2 keV which is still high enough above the Fe K edge. Note, that the emission above this region will have

quite low contribution to the overall spectral shape of the observed broadened line due to radial decrease of the line emissivity as  $r^{-3}$ .

We have computed the reflection from a neutral disc in constant density slab approximation by the Monte Carlo code NOAR (Dumont et al., 2000). The line flux was then computed by subtracting the interpolated reflected continuum from the reflection spectra. The line flux includes also the Compton shoulder created by scattering of the fluorescent photons before they leave the disc. We approximate the line with a narrow box function with a width of 1 eV (simulating a delta function) that has the numerically computed flux. This speeds up the code without loss of precision since the relativistically broadened line does not depend on the exact shape of the locally narrow line. The local Fe K $\alpha$  flux depends on incident and emission angles due to the fact that incident photon travels different distances in different layers during radiative transfer in the disc. On the other hand it does not depend on the azimuthal angle between incident and emitted light rays. We define the emission directionality function as the numerically computed flux in line per unit normalisation of the incident power-law flux

$$\mathcal{M}(\mu_i, \mu_e) \equiv \frac{dN}{dt dS^\perp d\Omega dE} = \frac{1}{2\pi \mu_e} \frac{\Delta N}{\Delta \mu_e \Delta E N_{\text{tot}}} \int_{E_0}^{E_c} E^{-\Gamma} dE, \quad (9)$$

where  $\Delta N$  is the number of photons emitted into the emission angle bin characterised by its cosine,  $\Delta \mu_e$ , i.e. into the whole azimuth of  $2\pi$ , hence the leading factor in the definition, and into energy bin  $\Delta E$ .  $N_{\text{tot}}$  is the total number of photons used in Monte Carlo computation and thus we multiply by the integrated energy dependence to normalise it as mentioned earlier, i.e. for incident power-law being exactly  $F_i(E) = E^{-\Gamma}$ . In the definition (9) there is one more factor of  $1/\mu_e$  due to the local flux being defined with respect to the area perpendicular to the emitted light ray while the reflected number of photons was computed per unit disc area. The sharp low,  $E_0$ , and high,  $E_c$ , energy cut-offs at 2 and 300 keV, respectively, were used in the computation. With this definition of emission directionality, the local line flux is defined as

$$F_{\text{loc}}(E) \equiv \mathcal{R}(r) \mathcal{M}(\mu_i, \mu_e) \delta(E - E_{\text{rest}}) \quad (10)$$

with  $E_{\text{rest}} = 6.4$  keV being the rest energy of the neutral Fe K $\alpha$  line and radial dependence of the normalisation of the incident power-law as discussed in the previous section,  $\mathcal{R}(r) = N_l N_i(r)$ , see eq. (1).

We show the emission directionality function,  $\mathcal{M}(\mu_i, \mu_e)$ , in the bottom panel of Fig. 3 for the photon index of the primary radiation  $\Gamma = 2$ . To see which values this function may acquire we also show the values of cosines of incident and emission angles at the top panel of the same figure (maps of cosine of emission angles are also shown in Figs. B1, B4 and B7). One can see that more radiation is emitted when the incident angle is large (measured from the normal to the disc), i.e. when the photons arrive almost parallelly with the disc. The same applies for the angular dependence of emissivity which obeys limb brightening law. The

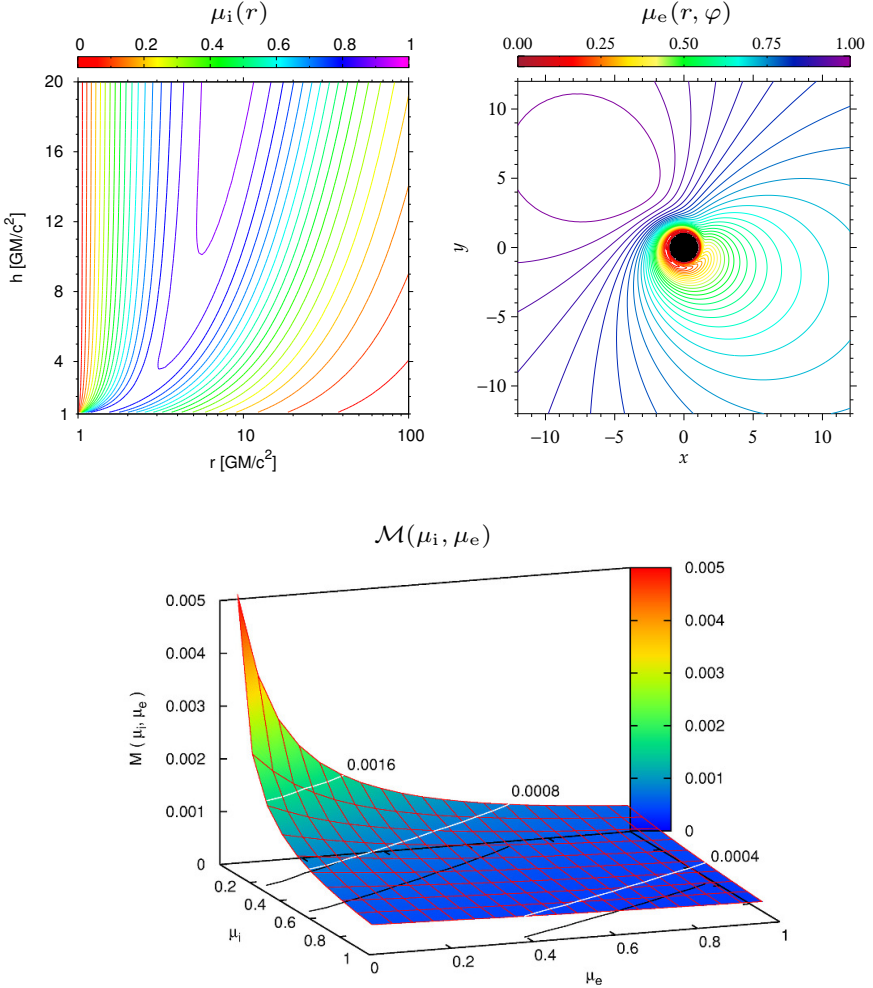


**Figure 3.** *Top left:* The radial dependence of the cosine of the incident angle,  $\mu_i$ , for different heights of the primary source and for the extremly rotating black hole with the spin  $a = 1 GM/c$ . *Top right:* The dependence of the cosine of the emission angle,  $\mu_e$ , on the position on the disc. The spin of the black hole is  $a = 1 GM/c$  and the inclination of the observer is  $\theta_o = 30^\circ$ . *Bottom:* The emission directionality function,  $\mathcal{M}(\mu_i, \mu_e)$ , is depicted for the photon index  $\Gamma = 2$ . Notice the high values it acquires for large incident and emission angles.

brightening is, however, smaller than the limb brightening law derived by Haardt and Matt (1993), where  $\mathcal{M}(\mu_e) \sim \ln(1 + \mu_e^{-1})$ . Since both the incident as well as emission angles are very high close above the horizon due to aberration caused by high Keplerian velocity, the emission directionality will be highest in this region. We

show the map of  $\mathcal{M}(\mu_i(r, \varphi), \mu_e(r, \varphi))$  in the equatorial plane for several values of black hole spin, observer inclination and height of the primary source in Figs. B2, B5 and B8. One can already appreciate the importance of the limb brightening effect by comparing the values of this function with the values of energy shift,  $g$ , and transfer function (i.e. the amplification of the local emission due to relativistic effects),  $G$ , shown in Figs. B1, B4 and B7. Thus we can expect that the shape of the broad iron line may be substantially influenced by the emission directionality. Moreover, the dependence of the emission directionality on the radius through the radially dependent incident and emission angles might cause that the observed radial emissivity profile, characterised by the radial power-law index  $q$ , might be measured with a systematic error if wrong assumption on emission directionality is taken (Svoboda et al., 2014).

#### 4 THE SHAPE OF THE RELATIVISTIC LINE IN LAMP-POST GEOMETRY

In the previous two sections we have discussed the local line flux and its dependence on the disc illumination, that gave us the radial part of the local emission, and local re-processing in the disc, that determined the emission directionality. The final shape of the observed spectral line is influenced by the relativistic effects that change the spectral properties of the local emission when transferred to the observer at infinity. The local spectrum will be shifted in energy due to Doppler shift and gravitational redshift, and it will be amplified due to Doppler boosting, gravitational lensing, aberration and light bending (the last two influence the local emission angle i.e. change the projections of the emitting area). To get the observed shape of the line one has to integrate the local emission over the whole disc

$$F_{\text{obs}}(E) \equiv \frac{dN_{\text{obs}}}{dt d\Omega dE} = \int dS G F_{\text{loc}} \delta(E - gE_{\text{rest}}), \quad (11)$$

where  $G$  is the transfer function (see e.g. Cunningham, 1975; Dovčiak, 2004) characterising an amplification of the local line flux,  $F_{\text{loc}} = \mathcal{R}(r)\mathcal{M}(\mu_i, \mu_e)$ , which is shifted to the observed energy by the  $g$ -factor,  $g = E/E_{\text{rest}}$ . Note, that the  $\delta$ -function in this equation is in the observed energy while in the eq. (10) it was in the local energy. The transfer function for a photon number density flux is  $G = g^2 l \mu_e$ , where the lensing,  $l$ , characterises amplification due to focusing of the light rays (caused by light bending). As mentioned in the previous sections, each part that contributes to the overall shape of the observed line,  $\mathcal{R}(r)$ ,  $\mathcal{M}(\mu_i, \mu_e)$ ,  $G(r, \varphi)$  as well as the energy shift  $g(r, \varphi)$  are depicted in the Appendices A and B. Additionally we also show the overall map of the observed flux  $F_{\text{obs}}(r, \varphi) = G \mathcal{R}(r)\mathcal{M}(\mu_i, \mu_e)$  in the equatorial plane in Figs. B3, B6 and B9. Note, that in the eq. (11) for each observed energy one integrates this function along the energy shift contour.

The shape of the relativistically broadened spectral line of iron for different assumptions on radial emissivity and emission directionality is shown in Fig. 4. One can see that the broken power-law emissivities result in quite a different line shape



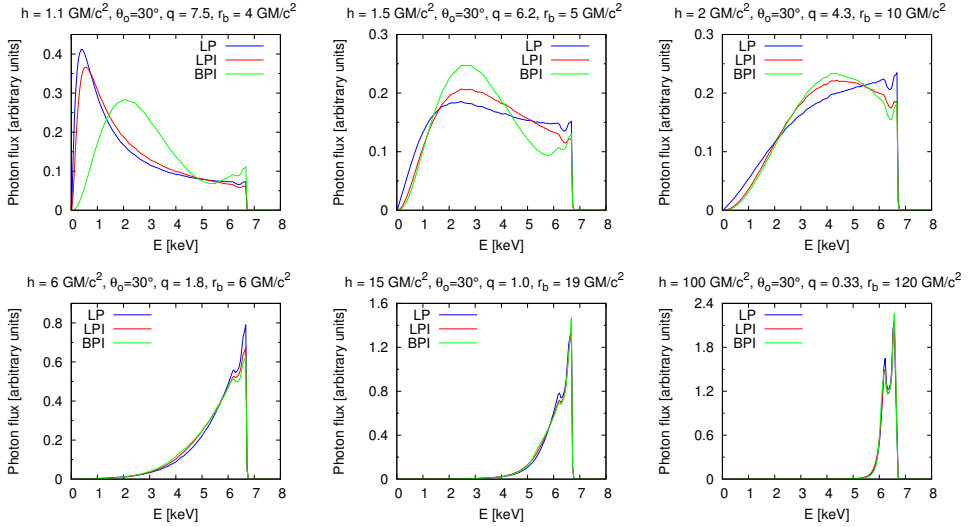


**Figure 4.** The comparison between the shape of the line in the lamp-post geometry with numerically computed angular directionality (blue) and with isotropic emission (red), and with the radial broken power-law emission with isotropic directionality (green). The height,  $h$ , the value of the inner radial power-law index,  $q$ , and the break radius,  $r_b$ , where it changes to  $q_{\text{out}} = 3$ , are shown at the top of each graph. The inclination of the observer is  $\theta_o = 30^\circ$ , the spin of the black hole is  $a = 1 \text{ GM}/c$  and the photon index of the primary source is  $\Gamma = 2$ .

only for a very low locations of the corona when compared with a lamp-post illumination profile, in both cases an isotropic local emission being assumed. The differences might be very well explained by comparing the emissivity profiles in Fig. A1. The broken power-law emissivity underestimates the flux, the largest deficiency occurs in the region very close to the black hole, where the gravitational redshift is large, and around the break radius,  $r_b$ . Note, that in Fig. 4 the line flux is in all cases normalised to unit total flux, so the spectral line for broken power-law radial profile is not below that one for the lamp-post geometry for all energies. One can see, however, that the line flux is much lower in two energy bands, one, where the energy shift is large with small values of  $g$ -factor,  $g \ll 1$ , (i.e. for low energies) and one when the  $g$ -factor is widely spread around unity (i.e. energies around iron line rest energy) that corresponds to the break radius region. Note, that the deficiency in the flux for low heights changes to an excess in flux for high heights of the primary source.

Further differences in the line shape arise when isotropic emission is compared with the numerically computed one given by the emission directionality function  $\mathcal{M}(\mu_i, \mu_e)$ . Again these differences are large only for low heights of the corona. The numerically computed directionality results in larger flux for low energies and energies around the rest energy of the line. This is mainly due the incident angle

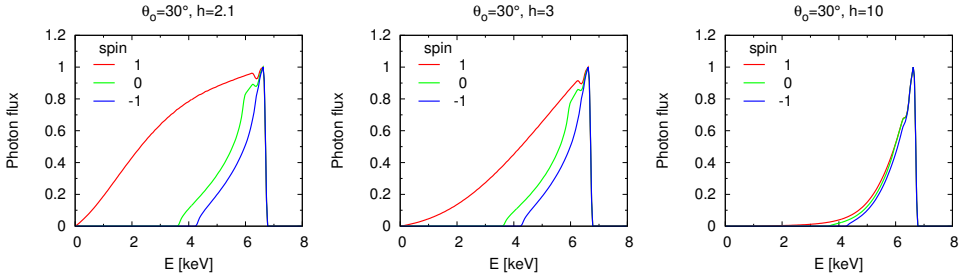


**Figure 5.** The comparison between the shape of the line in the lamp-post geometry for the Schwarzschild (green) and co-rotating (red) and counter-rotating (blue) extreme Kerr black holes for the primary source height,  $h = 2.1, 3$  and  $10 GM/c^2$ . The inclination of the observer is  $\theta_o = 30^\circ$  and the photon index of the primary source is  $\Gamma = 2$ .

being very high both in the vicinity of the black hole as well as farther away from the centre (see the top left panel in Fig. 3) when the emission directionality function acquires higher values (see the bottom panel in the same figure).

To see how the shape of the relativistically broadened line depends on the height of the source, let's compare the line for three different spins and three different heights (Fig. 5). One immediately sees that the line is much narrower for higher heights even for the extreme Kerr black hole. This is due to the fact that the disc is illuminated much more homogeneously from higher lamps and since the area of the inner part of the disc, where the red wing of the line arises, is very small compared to the area of the whole disc. Thus the shape of the line changes very little for different black hole spins if the corona is positioned more than  $10 GM/c^2$  above the centre. Opposite is also true, i.e. if the black hole counter-rotates with an extreme spin, one would not be able to distinguish between different heights of the corona if the height is below approximately  $10 GM/c^2$  above the centre. This is due to the fact that in this case the hole in the disc below marginally stable orbit ( $r_{\text{ms}} = 9 GM/c^2$ ) is quite large and the disc illumination for small heights of the primary source changes mainly below this radius while it does not change that much above the inner edge of the disc.

## 5 APPLICATION TO MCG-6-30-15

Using the computations from previous sections we have prepared a new XSPEC model for the relativistically broadened Iron line in the lamp-post geometry, see the Appendix C for more details. To find out what value of the height of the primary source one can expect in real observations where large spin have been observed in the past, we applied our new lamp-post model to the XMM-Newton spectrum of a nearby Seyfert 1 galaxy MCG-6-30-15. Very broad iron line was reported in this source by several authors (e.g. Fabian et al., 2002; Ballantyne et al., 2003; Vaughan and Fabian, 2003; Brenneman and Reynolds, 2006). We followed the analysis pre-

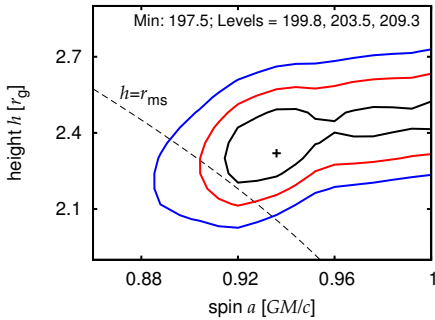


**Figure 6.** *Left:* The  $\chi^2$  contour graphs for the height,  $h$ , versus spin,  $a$ . Other parameters were kept frozen. *Right:* The best fit values and their errors for the parameters of the model.

sented in Svoboda et al. (2009) and we employed the same model for the underlying X-ray continuum. However, we have used the new KYNRLPLI model instead of the KYRLINE (Dovčiak et al., 2004b) so that we replaced the broken power-law radial emissivity by the one that corresponds to the lamp-post geometry. In XSPEC syntax the overall model reads: PHABS\*(POWERLAW+ZGAUSS+ZGAUSS+KYNRLPLI). The best-fit parameter values and their errors are shown in the table in the right panel of Fig. 6. The parameters not shown in the table were frozen to their best-fit values from the previous model set-up. The reduced  $\chi^2$  value was 1.33. The contour plot of the primary source height versus the black hole spin is shown in the left panel of Fig. 6. The best-fit value for the height,  $h = 2.3 GM/c^2$ , confirms our findings that if the primary source of power-law radiation is static, it has to be located very close to the black hole so that it illuminates the inner regions by large enough intensity to reveal the imprints of high spin in the observed spectrum.

## 6 CONCLUSIONS

In this paper we have compared two types of iron line radial emissivity profiles, the one governed by the illumination in the lamp-post geometry and the radial broken power-law emissivity. We find that

- for the primary source height  $h \gtrsim 3 GM/c^2$  the lamp-post geometry is very well approximated with the broken power-law emissivity with the inner power-law index  $q_{\text{in}} \lesssim 4$  and the outer index  $q_{\text{out}} = 3$ ,
- a very high radial power-law index,  $q > 5$ , may be achieved in the lamp-post geometry only for very small heights,  $h \lesssim 2 GM/c^2$ , and, the difference in the line shape in the lamp-post geometry and the broken power-law emissivity becomes large,
- very high  $q$  values originate very close to the central black hole, thus it can occur only in the case of a highly spinning black hole,

- high  $q$  values are mainly due to the gravitational redshift for the primary emission with the spectral index  $\Gamma > 1$  and due to the gravitational aberration for very small heights; the contribution of the light bending, as defined in this paper, is moderate.

Further we have investigated how the numerically computed emission directionality changes the profile of the iron line approximated by isotropic emission. We show that

- the emission from the disc where the incident and emission angles are large is greatly enhanced (limb brightening effect),
- the local emission directionality changes the shape of the broad line significantly, however, only for small heights,  $h \lesssim 10 GM/c^2$ .

To summarise our modelling we conclude that in the lamp-post geometry with a corona approximated by a static isotropic point source a very broad iron line profile arises for highly spinning black holes only for the heights  $h \lesssim 5 GM/c^2$ , while for the heights  $h \gtrsim 10 GM/c^2$  the non-spinning and extremely spinning black holes are indistinguishable.

Similar conclusions were drawn by Dauser et al. (2013) for a moving elongated jet-like structure along the axis. Another interesting conclusion in their paper is that such a vertically extended region may be very well approximated by a point source at some effective intermediate height. On the other hand, Wilkins and Fabian (2012) show that such steep emissivities may still be reached even if the corona is extended horizontally (as far as  $30 GM/c^2$ ), provided it is very low above the disc (as low as  $2 GM/c^2$ ). For a more detailed discussion on the prospects of spin determination using X-ray reflection we refer the reader to a recent paper by Fabian et al. (2014).

## ACKNOWLEDGEMENTS

The research leading to these results has received funding from the European Union Seventh Framework Programme (FP7/2007-2013) under grant agreement n°312789. RG would like to thank French GdR PCHE and the CNRS-AV exchange programme for their support. GM acknowledges financial support from Agenzia Spaziale Italiana (ASI).

## REFERENCES

- Arnaud, K. A. (1996), XSPEC: The First Ten Years, in G. H. Jacoby and J. Barnes, editors, *Astronomical Data Analysis Software and Systems V*, *A.S.P. Conference Series*, volume 101, p. 17.
- Ballantyne, D. R., Vaughan, S. and Fabian, A. C. (2003), A two-component ionized reflection model of MCG-6-30-15, *MNRAS*, **342**, p. 11.
- Biretta, J., Junor, W. and Livio, M. (2002), Evidence for initial jet formation by an accretion disk in the radio galaxy M87, *New Astronomy Reviews*, **46**, pp. 239–245.

- Blandford, R. D. and Znajek, R. L. (1977), Electromagnetic extraction of energy from Kerr black holes., *MNRAS*, **179**, pp. 433–456.
- Brenneman, L. W. and Reynolds, C. S. (2006), Constraining Black Hole Spin Via X-ray Spectroscopy, *ApJ*, **652**, p. 42.
- Cackett, E. M. and Miller, J. M. (2013), Broad iron lines in neutrons stars: dynamical broadening or wind scattering?, *ApJ*, **777**, p. 5.
- Cackett, E. M., Zoghbi, A., Reynolds, C., Fabian, A. C., Kara, E., Uttley, P. and Wilkins, D. R. (2014), Modelling the broad Fe K reverberation in the AGN NGC 4151, *MNRAS*, **438**, pp. 2980–2994.
- Cunningham, C. T. (1975), The effects of redshifts and focusing on the spectrum of an accretion disk around a Kerr black hole, *ApJ*, **202**, p. 788.
- Dauser, T., Garcia, J., Wilms, J., Bock, M., Brenneman, L. W., Falanga, M., Fukumura, K. and Reynolds, C. S. (2013), Irradiation of an accretion disc by a jet: general properties and implications for spin measurements of black holes, *MNRAS*, **430**, pp. 1694–1708.
- Dovčiak, M. (2004), *Radiation of Accretion Discs in Strong Gravity*, PhD thesis, Charles University, Prague.
- Dovčiak, M., Karas, V., Martocchia, A., Matt, G. and Yaqoob, T. (2004a), An XSPEC model to explore spectral features from black-hole sources, in *Proceedings of RAGtime: Workshops on black holes and neutron stars*, volume 4/5, p. 35.
- Dovčiak, M., Karas, V. and Yaqoob, T. (2004b), An Extended Scheme for Fitting XRay Data with Accretion Disk Spectra in the Strong Gravity Regime, *ApJS*, **153**, pp. 205–221.
- Dovčiak, M., Muleri, F., Goosmann, R. W., Karas, V. and Matt, G. (2011), Light bending scenario for accreting black holes in X-ray polarimetry, *ApJ*, **731**, p. 17.
- Dumont, A. M., Abrassart, A. and Collin, S. (2000), A code for optically thick and hot photoionized media, *A&A*, **357**, p. 17.
- Emmanoulopoulos, D., Papadakis, I. E., Dovčiak, M. and McHardy, I. M. (2014), General relativistic modelling of the negative reverberation X-ray time delays in AGN, *MNRAS*, **439**, pp. 3931–3950.
- Fabian, A. C., Kara, E., Walton, D. J., Wilkins, D. R., Ross, R. R., Lozanov, K., Uttley, P., Gallo, L. C., Zoghbi, A., Miniutti, G., Boller, T., Brandt, W. N., Cackett, E. M., Chiang, C.-Y., Dwelly, T., Malzac, J., Miller, J. M., Nardini, E., Ponti, G., Reis, R. C., Reynolds, C. S., Steiner, J., Tanaka, Y. and Young, A. J. (2013), Long XMM observation of the Narrow-Line Seyfert 1 galaxy IRAS13224-3809: rapid variability, high spin and a soft lag, *MNRAS*, **429**, p. 7.
- Fabian, A. C., Parker, M. L., Wilkins, D. R., Miller, J. M., Kara, E., Reynolds, C. S. and Dauser, T. (2014), On the determination of the spin and disc truncation of accreting black holes using X-ray reflection, *MNRAS*, **439**, pp. 2307–2313.
- Fabian, A. C., Rees, M. J., Stella, L. and White, N. E. (1989), X-ray fluorescence from the inner disc in Cygnus X-1, *MNRAS*, **238**, pp. 729–736.
- Fabian, A. C., Vaughan, S., Nandra, K., Iwasawa, K., Ballantyne, D. R., Lee, J. C., De Rosa, A., Turner, A. and Young, A. J. (2002), A long hard look at MCG-6-30-15 with XMM-Newton, *MNRAS*, **335**, p. 5.
- Fabian, A. C., Zoghbi, A., Ross, R. R., Uttley, P., Gallo, L. C., Brandt, W. N., Blustin, A. J., Boller, T., Caballero-Garcia, M. D., Larsson, J., Miller, J. M., Miniutti, G., Ponti, G., Reis, R. C., Reynolds, C. S., Tanaka, Y. and Young, A. J. (2009), Broad line emission from iron K- and L-shell transitions in the active galaxy 1H 0707-495., *Nature*,

**459**, pp. 540–2.

- Fabian, A. C., Zoghbi, A., Wilkins, D., Dwelly, T., Uttley, P., Schartel, N., Miniutti, G., Gallo, L., Grupe, D., Komossa, S. and Santos-Lleo, M. (2011), 1H0707-495 in 2011: An X-ray source within a gravitational radius of the event horizon, *MNRAS*, **419**, p. 9.
- Frank, J., King, A. and Raine, D. J. (2002), *Accretion Power in Astrophysics*, UK: Cambridge University Press, Cambridge, third edition, ISBN 0521620538.
- García, J., Dauser, T., Reynolds, C. S., Kallman, T. R., McClintock, J. E., Wilms, J. and Eikmann, W. (2013), X-ray reflected spectra from accretion disk models. III. A complete grid of ionized reflection calculations, *ApJ*, **768**, p. 146.
- Ghisellini, G., Haardt, F. and Matt, G. (2004), Aborted jets and the X-ray emission of radio-quiet AGNs, *A&A*, **413**, p. 11.
- Haardt, F. and Matt, G. (1993), X-ray polarization in the two-phase model for AGN and X-ray binaries, *MNRAS*, **261**, pp. 346–352.
- Martocchia, A. and Matt, G. (1996), Iron Kalpha line intensity from accretion discs around rotating black holes, *MNRAS*, **282**, pp. L53–L57.
- Matt, G., Perola, G. C. and Piro, L. (1991), The iron line and high energy bump as X-ray signatures of cold matter in Seyfert 1 galaxies., *A&A*, **247**, pp. 25–34.
- Miller, J. M., Parker, M. L., Fuerst, F., Bachetti, M., Harrison, F. A., Barret, D., Boggs, S. E., Chakrabarty, D., Christensen, F. E., Craig, W. W., Fabian, A. C., Grefenstette, B. W., Hailey, C. J., King, A. L., Stern, D. K., Tomsick, J. A., Walton, D. J. and Zhang, W. W. (2013), NuSTAR Spectroscopy of GRS 1915+105: Disk Reflection, Spin, and Connections to Jets, *ApJ*, **775**, p. L45.
- Miller, L. and Turner, T. J. (2013), The hard X-ray spectrum of NGC 1365: scattered light, not black hole spin, *ApJ*, **773**, p. L5.
- Miniutti, G. and Fabian, A. C. (2004), A light bending model for the X-ray temporal and spectral properties of accreting black holes, *MNRAS*, **349**, pp. 1435–1448.
- Mirabel, I. F. and Rodríguez, L. F. (1998), Microquasars in our Galaxy, *Nature*, **392**, pp. 673–676.
- Niedźwiecki, A. and Miyakawa, T. (2010), General relativistic models of the X-ray spectral variability of MCG6-30-15, *A&A*, **509**, p. A22.
- Peterson, B. M. (1997), *An Introduction to Active Galactic Nuclei*, New York Cambridge University Press, Cambridge, ISBN 0521473489.
- Ponti, G., Gallo, L. C., Fabian, A. C., Miniutti, G., Zoghbi, A., Uttley, P., Ross, R. R., Vasudevan, R. V., Tanaka, Y. and Brandt, W. N. (2009), Relativistic disc reflection in the extreme NLS1 IRAS13224-3809, *MNRAS*, **406**, pp. 2591–2604.
- Risaliti, G., Harrison, F. A., Madsen, K. K., Walton, D. J., Boggs, S. E., Christensen, F. E., Craig, W. W., Grefenstette, B. W., Hailey, C. J., Nardini, E., Stern, D. and Zhang, W. W. (2013), A rapidly spinning supermassive black hole at the centre of NGC 1365, *Nature*, **494**, p. 22.
- Ross, R. R. and Fabian, A. C. (2005), A comprehensive range of X-ray ionized reflection models, *MNRAS*, **358**, p. 6.
- Svoboda, J., Dovčiak, M., Goosmann, R. and Karas, V. (2009), Role of emission angular directionality in spin determination of accreting black holes with a broad iron line, *A&A*, **507**, pp. 1–17.
- Svoboda, J., Dovčiak, M., Goosmann, R. W., Jethwa, P., Karas, V., Miniutti, G. and Guainazzi, M. (2012), Origin of the X-ray disc-reflection steep radial emissivity, *A&A*, **545**, p. 10.

- Svoboda, J., Dovčiak, M., Goosmann, R. W. and Karas, V. (2014), On the interplay between radial and angular reflection emissivity from the black hole accretion disc, in J. Bičák and T. Ledvinka, editors, *Relativity and Gravitation, Springer Proceedings in Physics*, volume 157 of *Springer Proceedings in Physics*, pp. 415–422, Springer International Publishing, Cham, ISBN 978-3-319-06760-5.
- Vaughan, S. and Fabian, A. C. (2003), A long, hard look at MCG-6-30-15 with XMM-Newton II: detailed EPIC analysis and modelling, *MNRAS*, **348**, p. 25.
- Verner, D., Yakovlev, D., Band, I. and Trzhaskovskaya, M. (1993), Subshell Photoionization Cross Sections and Ionization Energies of Atoms and Ions from He to Zn, *Atomic Data and Nuclear Data Tables*, **55**, pp. 233–280.
- Wilkins, D. R. and Fabian, A. C. (2011), Determination of the X-ray reflection emissivity profile of 1H 0707-495, *MNRAS*, **414**, p. 9.
- Wilkins, D. R. and Fabian, A. C. (2012), Understanding X-ray reflection emissivity profiles in AGN: locating the X-ray source, *MNRAS*, **424**, pp. 1284–1296.
- Wilms, J., Reynolds, C. S., Begelman, M. C., Reeves, J., Molendi, S., Stuabert, R. and Kendziorra, E. (2001), XMM-EPIC observation of MCG-6-30-15: Direct evidence for the extraction of energy from a spinning black hole?, *MNRAS*, **328**, p. 6.

## APPENDIX A: THE RADIAL ILLUMINATION PROFILE

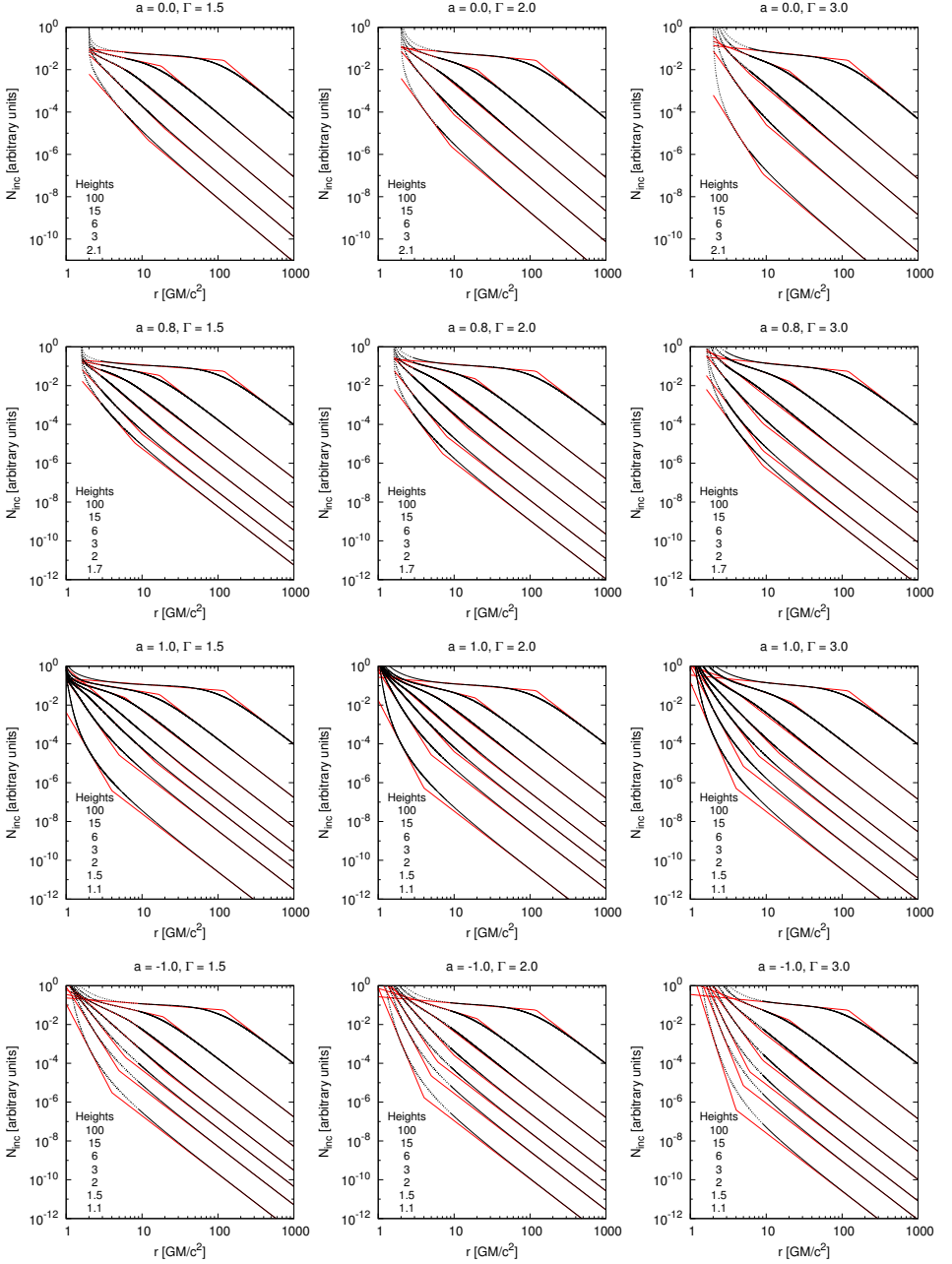


**Figure A1.** The radial profile of the incident flux,  $N_{\text{i}}(r)$ , defined in eq. (2), for the photon index  $\Gamma = 1.5, 2$  and  $3$  (left to right) and the BH spin  $a = 0, 0.8, 1$  and  $-1 \text{ GM}/c$  (top to bottom). For better clarity, the results shown for different heights, as depicted in each panel, are renormalized so as not to cross. The red lines represent the approximating broken-power-law profiles with the outer slope set to  $-3$  (see the Tab. A1-A4 for details).



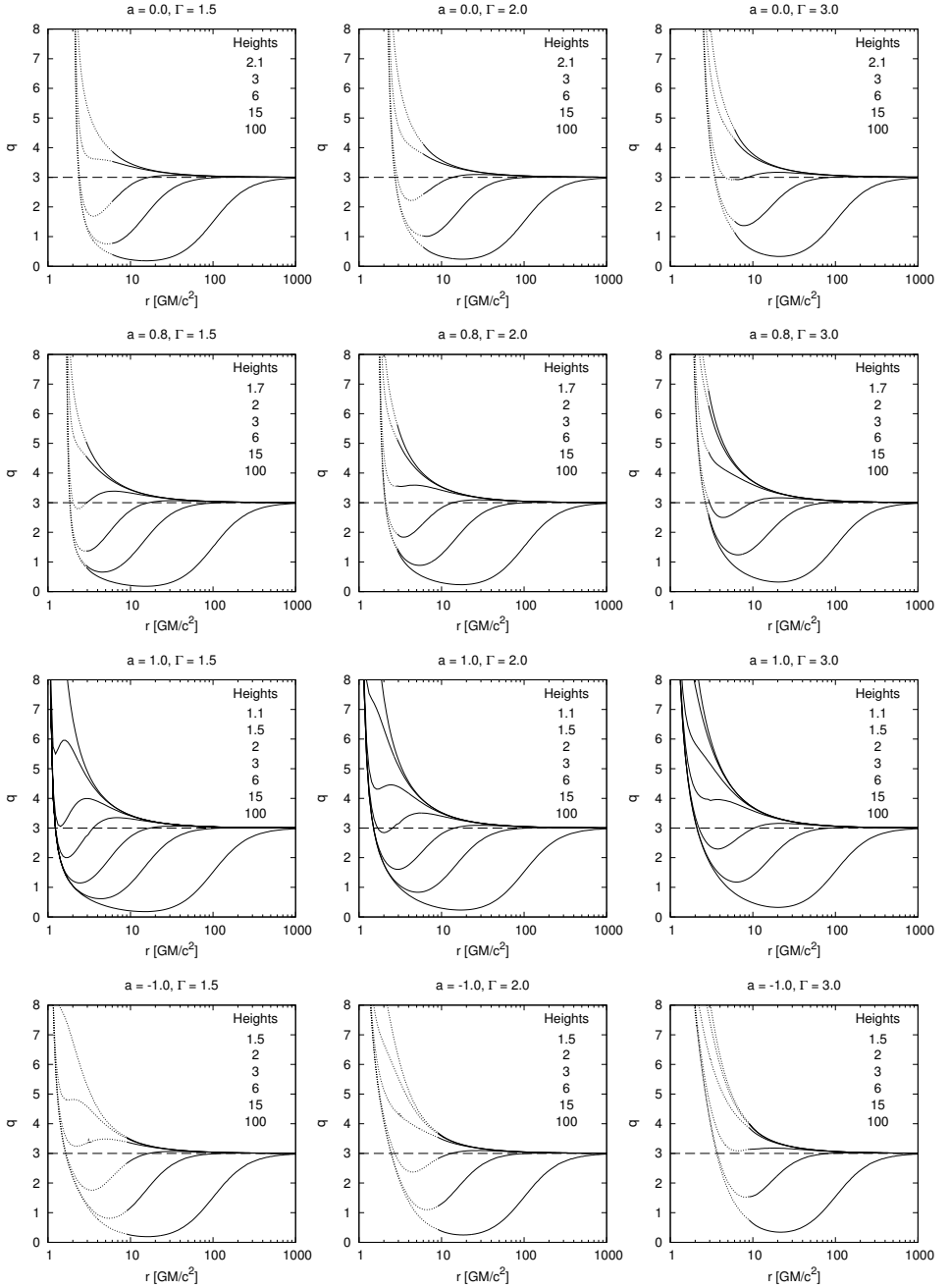


**Figure A2.** The radial dependence of the power-law index  $q(r)$ , defined in eq. (8), for the photon index  $\Gamma = 1.5, 2$  and  $3$  (left to right) and the BH spin  $a = 0, 0.8, 1$  and  $-1 \text{ GM}/c$  (top to bottom). The results for different heights, as depicted on each panel, are shown by solid lines above and by dotted lines below the marginally stable orbit.

$a = 0$						
$\Gamma$	1.5		2		3	
$h$	$q_i$	$r_b$	$q_i$	$r_b$	$q_i$	$r_b$
100	0.3	120	0.33	120	0.39	120
15	0.8	18	1.1	20	1.4	20
6	1.8	7	2.3	6	3.7	6
3	3.5	20	4.3	10	5.0	10
2.1	4.0	12	4.9	9	5.7	9

**Table A1.** The values of the inner slope for the broken power-law,  $q_i$ , and the break radius,  $r_b$ , for different height,  $h$ , (rows) and photon index,  $\Gamma$ , (columns) in the case of a non-rotating Schwarzschild black hole (with the spin  $a = 0 \, GM/c$ , horizon  $r_h = 2 \, GM/c^2$  and marginally stable orbit  $r_{ms} = 6 \, GM/c^2$ ). Both the height and the break radius are specified in units of  $GM/c^2$ . These values correspond to the broken power-law dependences in the top panels in Fig. A1.

$a = 0.8$						
$\Gamma$	1.5		2		3	
$h$	$q_i$	$r_b$	$q_i$	$r_b$	$q_i$	$r_b$
100	0.3	120	0.33	120	0.39	120
15	0.7	17	1.0	19	1.4	20
6	1.6	7	2.0	6	3.1	8
3	3.4	20	3.7	15	4.7	9
2	4.2	10	4.9	8	5.2	9
1.7	4.6	8	5.2	7	5.3	9

**Table A2.** The same as in Table A1 but for the co-rotating Kerr black hole with the spin  $a = 0.8 \, GM/c$  (horizon  $r_h = 1.6 \, GM/c^2$  and marginally stable orbit  $r_{ms} = 2.9 \, GM/c^2$ ). These values correspond to the broken power-law dependences in the second row panels in Fig. A1.

$a = 1$						
$\Gamma$	1.5		2		3	
$h$	$q_i$	$r_b$	$q_i$	$r_b$	$q_i$	$r_b$
100	0.3	120	0.33	120	0.39	120
15	0.65	17	1.0	19	1.4	21
6	1.3	6	1.8	6	2.6	4
3	3.3	35	3.4	22	4.0	15
2	3.8	15	4.3	10	5.3	8
1.5	5.6	5	6.2	5	7.4	5
1.1	6.7	4	7.5	4	9.1	4

**Table A3.** The same as in Table A1 but for the extreme co-rotating Kerr black hole (with the spin  $a = 1 \text{ } GM/c$ , horizon  $r_h = 1 \text{ } GM/c^2$  and marginally stable orbit  $r_{\text{ms}} = 1 \text{ } GM/c^2$ ). These values correspond to the broken power-law dependences in the third row panels in Fig. A1.

$a = -1$						
$\Gamma$	1.5		2		3	
$h$	$q_i$	$r_b$	$q_i$	$r_b$	$q_i$	$r_b$
100	0.3	120	0.33	120	0.39	120
15	0.9	19	1.2	20	1.5	20
6	1.9	7	2.6	6	3.6	9
3	3.5	20	4.3	10	5.4	9
2	5.0	6	6.0	6	7.8	6
1.5	6.2	5	7.4	5	9.7	5
1.1	7.6	4	9.4	4	12.4	4

**Table A4.** The same as in Table A1 but for the extreme counter-rotating Kerr black hole (with the spin  $a = -1 \text{ } GM/c$ , horizon  $r_h = 1 \text{ } GM/c^2$  and marginally stable orbit  $r_{\text{ms}} = 9 \text{ } GM/c^2$ ). These values correspond to the broken power-law dependences in the bottom panels in Fig. A1.

## APPENDIX B: MAPS OF THE TRANSFER FUNCTION, EMISSION DIRECTIONALITY AND OBSERVED FLUX

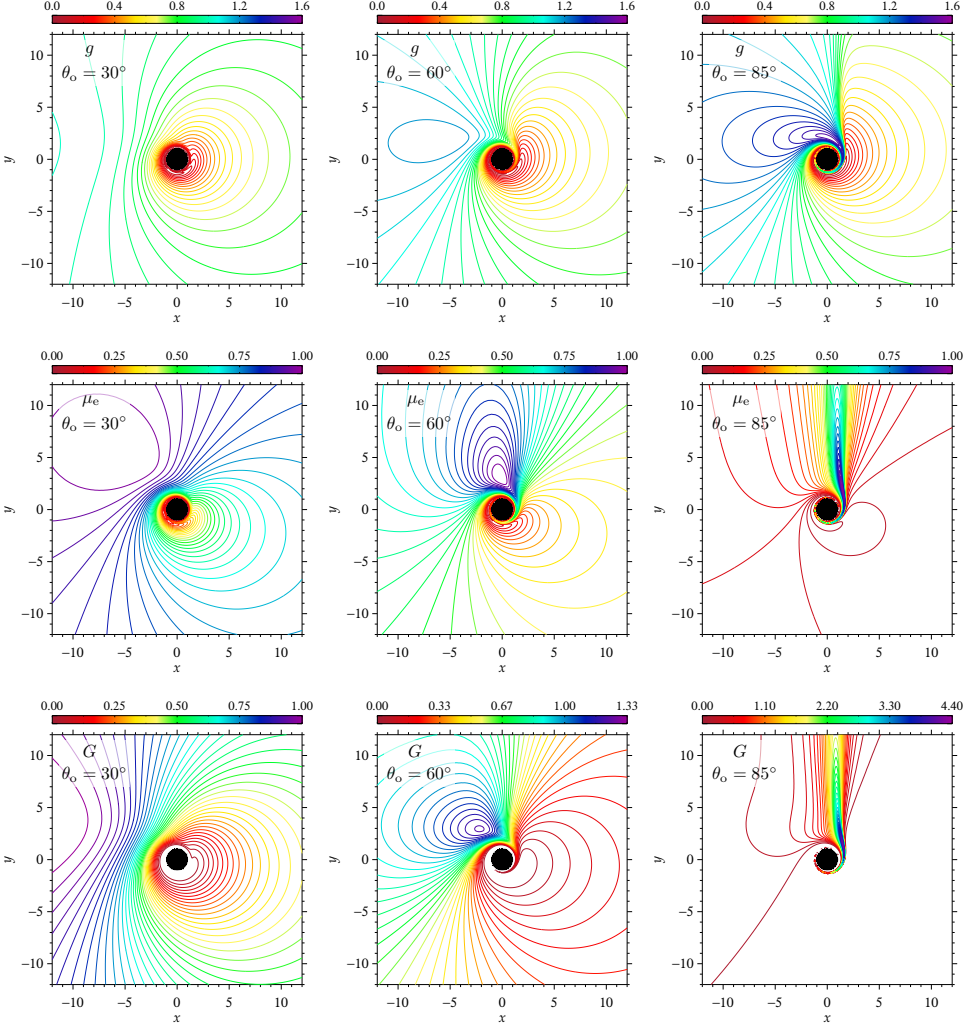


**Figure B1.** The equatorial plane map of the energy shift,  $g$ , cosine of emission angle,  $\mu_e$ , and transfer function,  $G$ , (top to bottom) for the co-rotating Kerr black hole ( $a = 1 GM/c$ ) and three inclination angles,  $\theta_o = 30^\circ$ ,  $60^\circ$  and  $85^\circ$  (left to right).

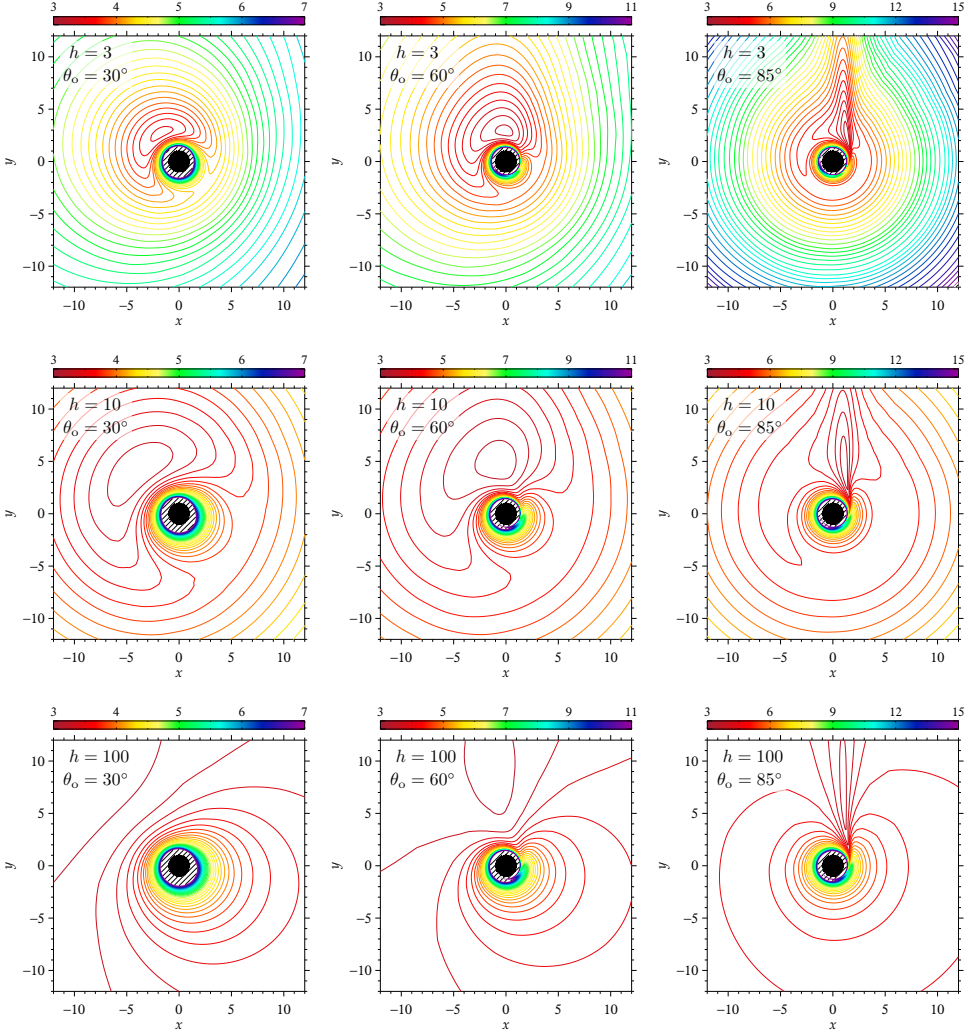


**Figure B2.** The equatorial plane map of the local flux emission directionality,  $\mathcal{M}(\mu_i, \mu_e)$ , for the co-rotating Kerr black hole ( $a = 1 GM/c$ ) and three inclination angles,  $\theta_o = 30^\circ, 60^\circ$  and  $85^\circ$  (left to right), and three heights of the primary source,  $h = 3, 10$  and  $100 GM/c^2$  (top to bottom).

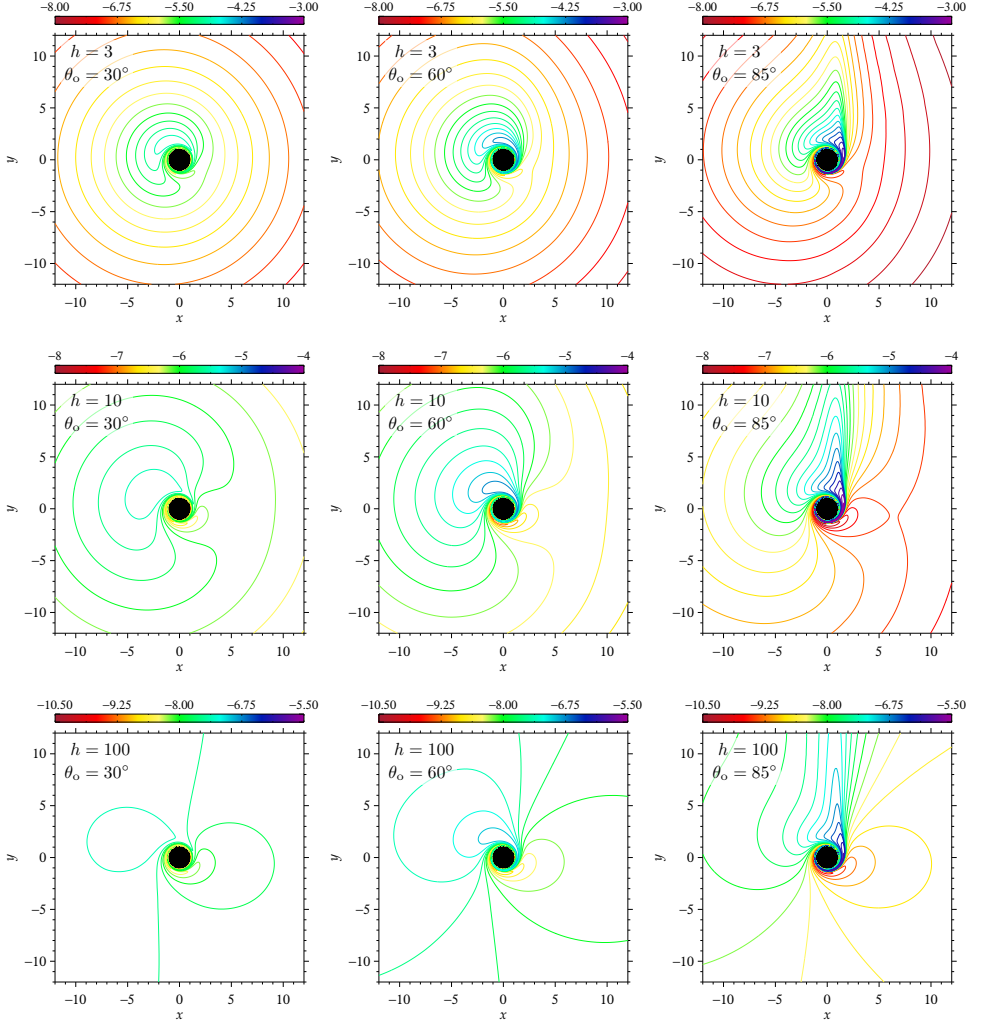


**Figure B3.** The equatorial plane map of the observed line flux,  $F_{\text{obs}}(r, \varphi)$ , for the corotating Kerr black hole ( $a = 1 \text{ GM}/c$ ) and three inclination angles,  $\theta_o = 30^\circ$ ,  $60^\circ$  and  $85^\circ$  (left to right), and three heights of the primary source,  $h = 3, 10$  and  $100 \text{ GM}/c^2$  (top to bottom).

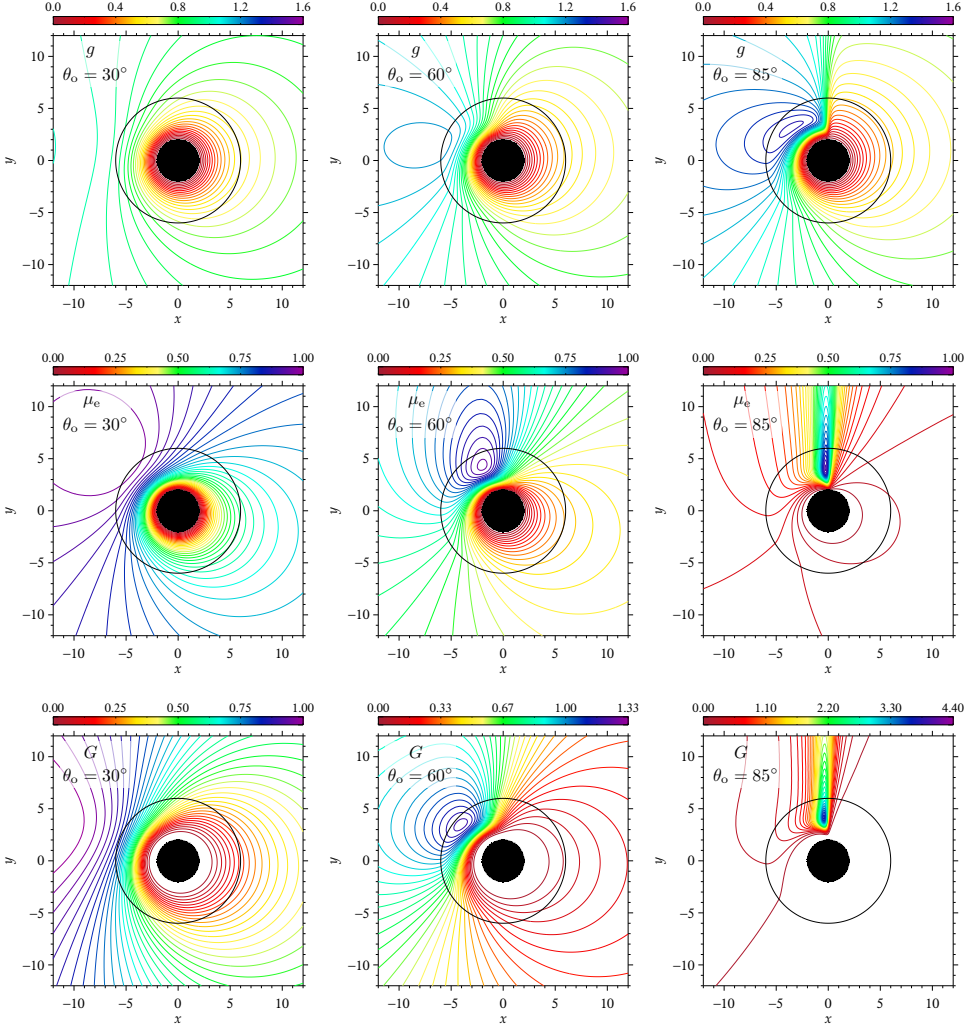


**Figure B4.** The equatorial plane map of the energy shift,  $g$ , cosine of emission angle,  $\mu_e$ , and transfer function,  $G$ , (top to bottom) for the Schwarzschild black hole ( $a = 0 \text{ GM}/c$ ) and three inclination angles,  $\theta_o = 30^\circ$ ,  $60^\circ$  and  $85^\circ$  (left to right). The marginally stable orbit at  $r_{\text{ms}} = 6 \text{ GM}/c^2$  is denoted by a black circle.

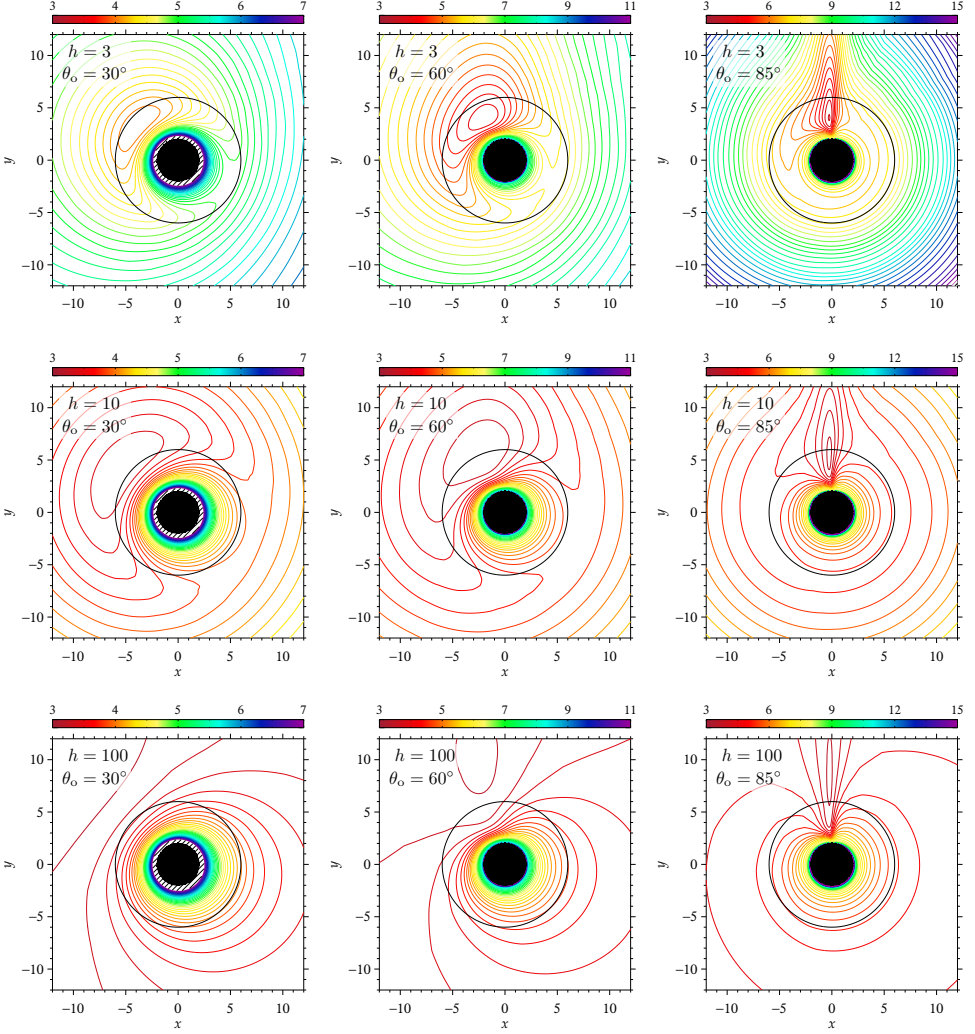


**Figure B5.** The equatorial plane map of the local flux emission directionality,  $\mathcal{M}(\mu_i, \mu_e)$ , for the Schwarzschild black hole ( $a = 0 \text{ GM}/c$ ) and three inclination angles,  $\theta_o = 30^\circ$ ,  $60^\circ$  and  $85^\circ$  (left to right), and three heights of the primary source,  $h = 3, 10$  and  $100 \text{ GM}/c^2$  (top to bottom). The marginally stable orbit at  $r_{\text{ms}} = 6 \text{ GM}/c^2$  is denoted by a black circle.



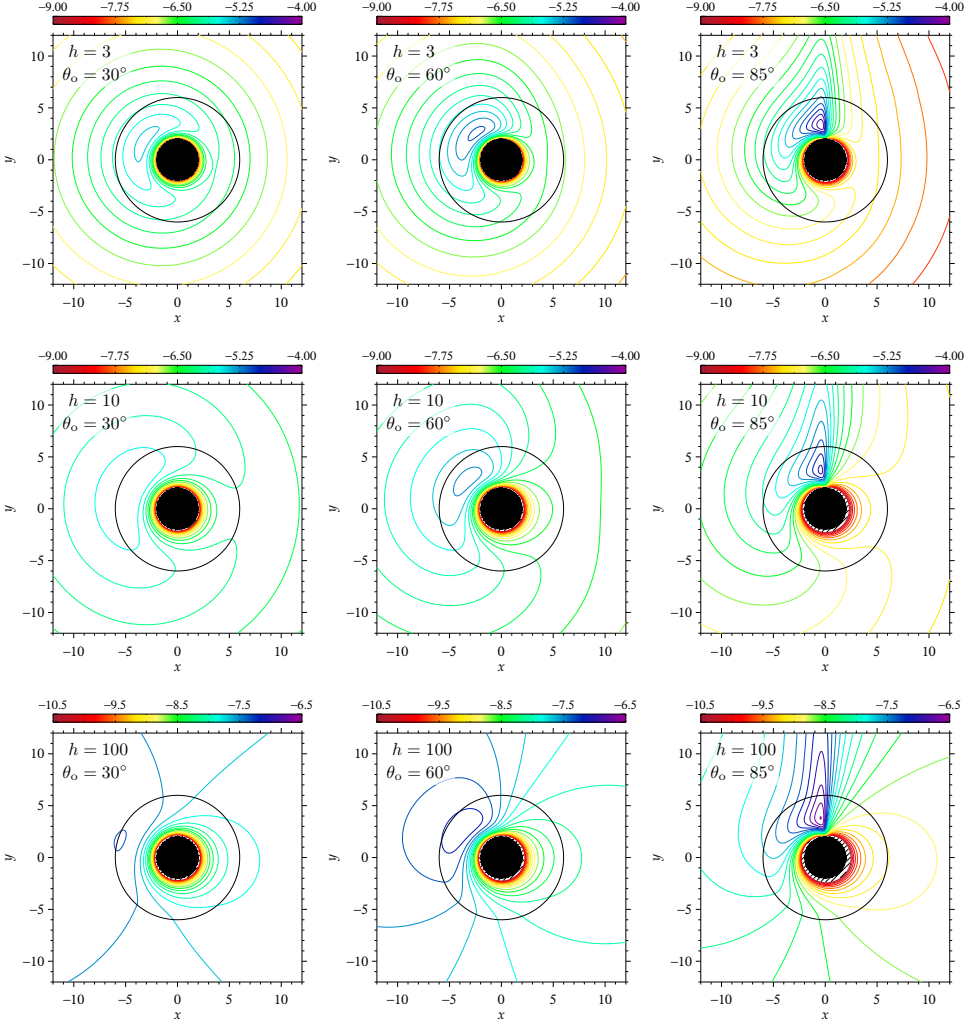


**Figure B6.** The equatorial plane map of the observed line flux,  $F_{\text{obs}}(r, \varphi)$ , for the Schwarzschild black hole ( $a = 0 \text{ GM}/c$ ) and three inclination angles,  $\theta_o = 30^\circ, 60^\circ$  and  $85^\circ$  (left to right), and three heights of the primary source,  $h = 3, 10$  and  $100 \text{ GM}/c^2$  (top to bottom). The marginally stable orbit at  $r_{\text{ms}} = 6 \text{ GM}/c^2$  is denoted by a black circle.

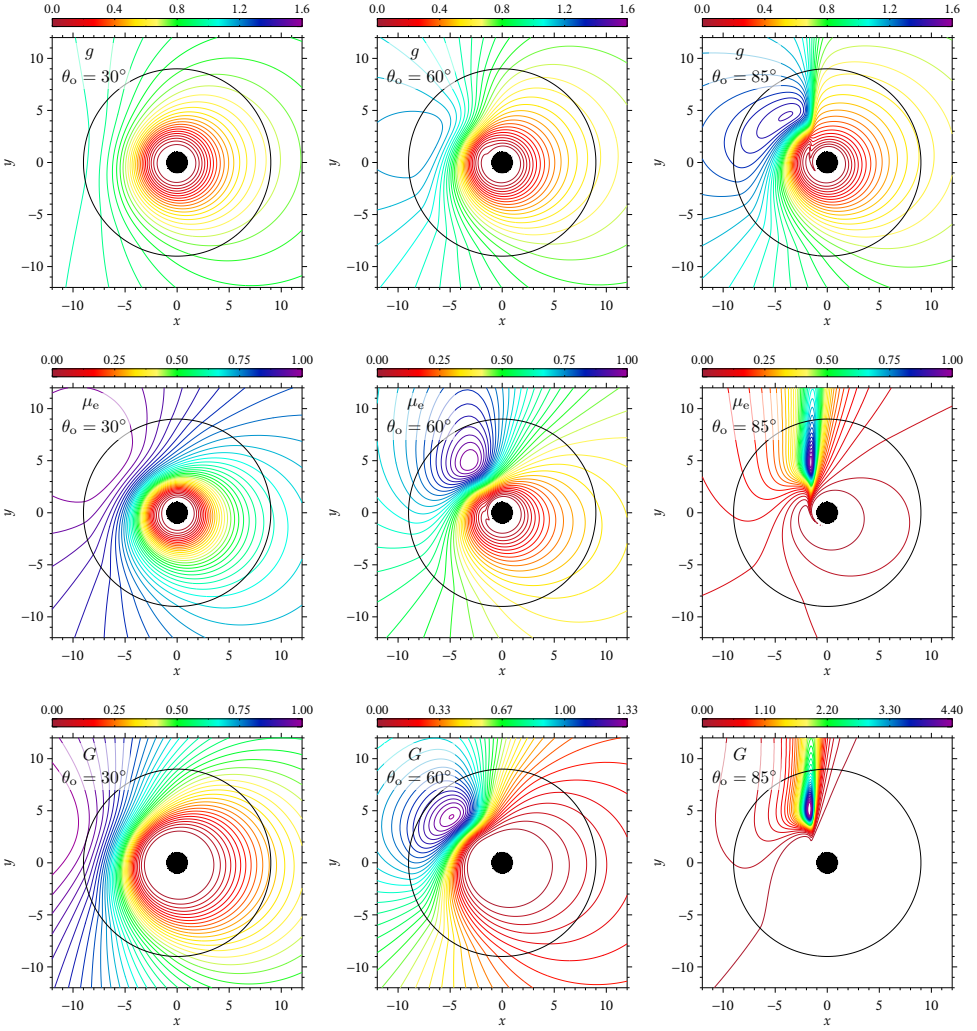


**Figure B7.** The equatorial plane map of the energy shift,  $g$ , cosine of emission angle,  $\mu_e$ , and transfer function,  $G$ , (top to bottom) for the counter-rotating Kerr black hole ( $a = -1 \text{ GM}/c$ ) and three inclination angles,  $\theta_o = 30^\circ$ ,  $60^\circ$  and  $85^\circ$  (left to right). The marginally stable orbit at  $r_{\text{ms}} = 9 \text{ GM}/c^2$  is denoted by a black circle.

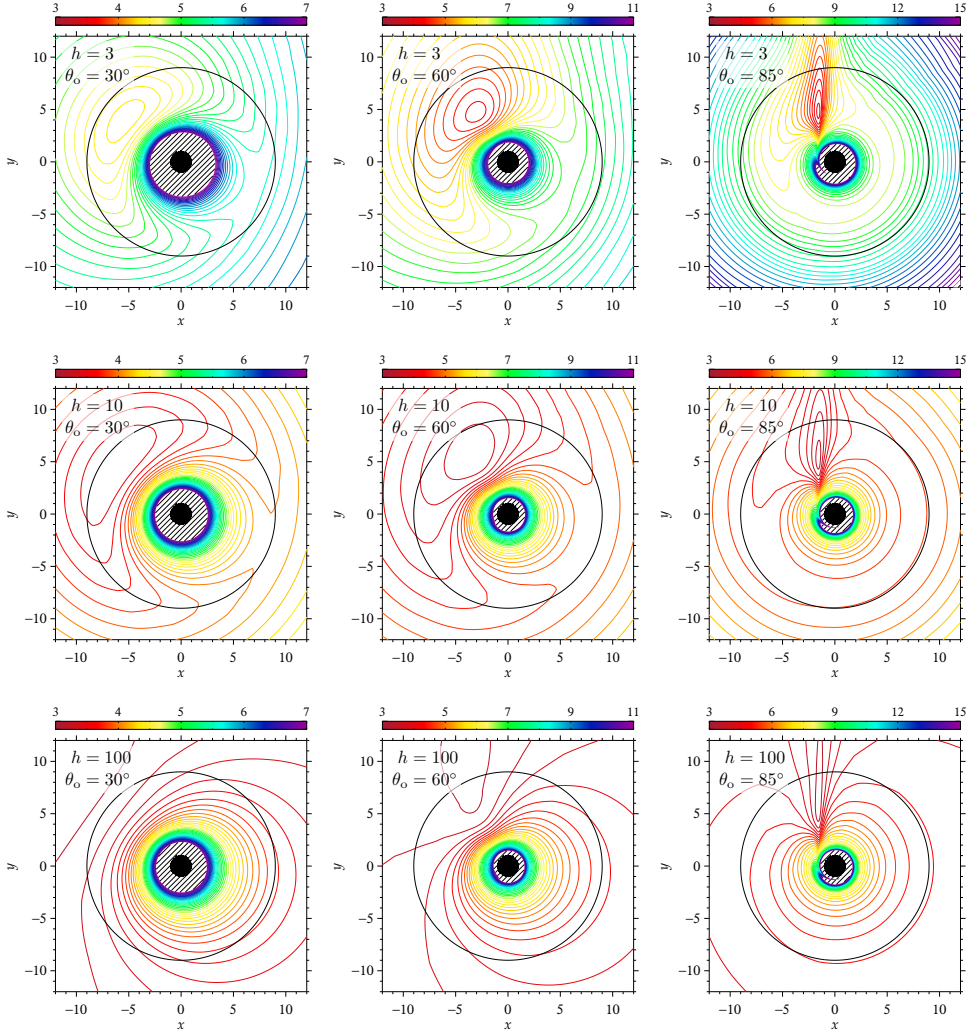


**Figure B8.** The equatorial plane map of the local flux emission directionality,  $\mathcal{M}(\mu_i, \mu_e)$ , for the counter-rotating Kerr black hole ( $a = -1 GM/c$ ) and three inclination angles,  $\theta_o = 30^\circ, 60^\circ$  and  $85^\circ$  (left to right), and three heights of the primary source,  $h = 3, 10$  and  $100 GM/c^2$  (top to bottom). The marginally stable orbit at  $r_{\text{ms}} = 9 GM/c^2$  is denoted by a black circle.

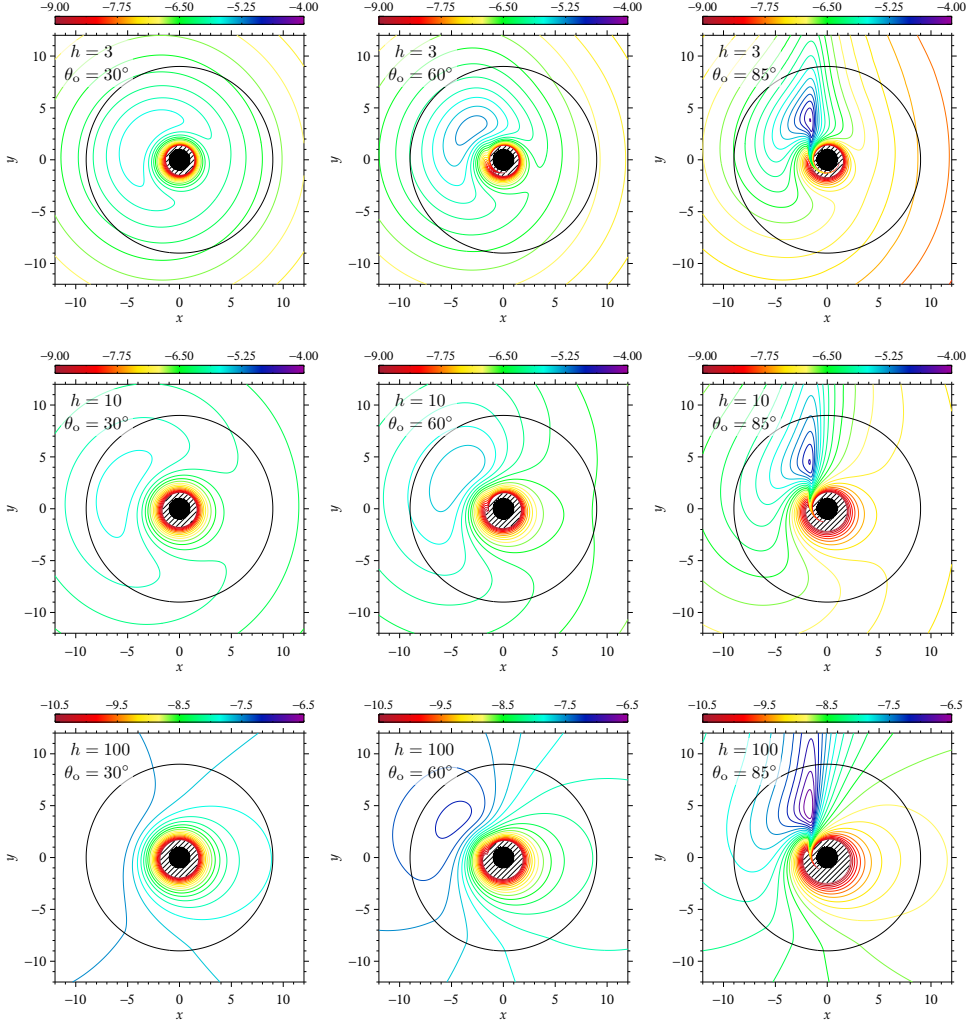


**Figure B9.** The equatorial plane map of the observed line flux,  $F_{\text{obs}}(r, \varphi)$ , for the counter-rotating Kerr black hole ( $a = -1 \text{ GM}/c$ ) and three inclination angles,  $\theta_o = 30^\circ, 60^\circ$  and  $85^\circ$  (left to right), and three heights of the primary source,  $h = 3, 10$  and  $100 \text{ GM}/c^2$  (top to bottom). The marginally stable orbit at  $r_{\text{ms}} = 9 \text{ GM}/c^2$  is denoted by a black circle.

# APPENDIX C: THE RELATIVISTIC IRON LINE MODEL FOR THE LAMP-POST GEOMETRY

To be able to use the lamp-post scheme with the data we have developed the model for XSPEC (Arnaud, 1996) – KYNRLPLI (KY Non-axisymmetric Relativistic Lamp-Post Line). This model is based on the non-axisymmetric version of the KY package of models (Dovčiak et al., 2004a,b; Dovčiak, 2004).

The model approximates the corona above the disc by a static isotropic point source located on the rotational axis at height,  $h$ , above the disc (measured from the centre of the black hole). Thus the radial emissivity profile is given by the illumination from such corona. All relativistic effects are taken into account all the way from the primary source to the disc and from the disc to the observer.

The local flux angular dependence,  $\mathcal{M}(\mu_i, \mu_e)$ , is computed with the Monte Carlo code NOAR (Dumont et al., 2000), see also Fig. 3 and Appendix B.

As is usual in non-axisymmetric KY models, it is possible to choose that the radiation comes only from a segment of the disc to simulate an emission from a spot. The inner and outer radius might be set either in physical units of  $GM/c^2$  or as a multiple of the marginally stable orbit,  $r_{\text{ms}}$ .

On the other hand we have added a possibility to obscure part of the disc by a circular cloud in the observer’s sky (i.e. farther away from the centre). The centre of the cloud is set in impact parameters,  $\alpha$  and  $\beta$ , where  $\alpha$  is positive for approaching side of the disc and  $\beta$  is positive above the black hole and negative below it (in the observer’s sky).

param. number	param.	unit	possible values	description
par1	$a$	$GM/c$	-1 – 1	black hole angular momentum
par2	$\theta_o$	deg	0 – 89	observer inclination (0° – pole, 90° – disc)
par3	$r_{\text{in}}$	$GM/c^2$	1 – 1000	inner disc edge
par4	ms		0, 1, 2	changes definition of inner edge 0: $r_{\text{in}} = \text{par3}$ 1: $r_{\text{in}} = \text{par3}$ but if $\text{par3} < r_{\text{ms}}$ then $r_{\text{in}} = r_{\text{ms}}$ 2: $r_{\text{in}} = \text{par3} \times r_{\text{ms}}$ , $r_{\text{out}} = \text{par5} \times r_{\text{ms}}$
par5	$r_{\text{out}}$	$GM/c^2$	1 – 1000	outer disc edge
par6	$\varphi_o$	deg	-180 – 180	lower azimuth of the disc segment
par7	$\Delta\varphi$	deg	0 – 360	width of the disc segment
par8	$h$	$GM/c^2$	1 – 100	height (location) of the primary
par9	$\Gamma$		1.1 – 3	primary energy power-law index

**Table C1.** Description of the KYNRLPLI parameters par1 – par9.

param. number	param.	unit	possible values	description
par10	$\alpha_c$	$GM/c^2$		$\alpha$ -position of the obscuring cloud
par11	$\beta_c$	$GM/c^2$		$\beta$ -position of the obscuring cloud
par12	$r_c$	$GM/c^2$		radius of the obscuring cloud
par13	zshift			overall Doppler shift
par14	ntable		80	defines fits file with tables
par15	$n_r$		$1 - 10^4$	number of radial grid points
par16	division		0, 1	type of step in radial integration (0 – equidistant, 1 – exponential)
par17	$n_\varphi$		$1 - 2 \times 10^4$	number of azimuthal grid points
par18	smooth		0, 1	smooth the resulting spectrum (0 – no, 1 – yes)
par19	Stokes		0 – 6	output of the computation: 0: photon number density flux (Stokes parameter I/E) 1: Stokes parameter Q/E 2: Stokes parameter U/E 3: Stokes parameter V/E 4: degree of polarization 5: linear polarization angle, $\chi = \frac{1}{2} \operatorname{atan} \frac{U}{Q}$ 6: circular polarization angle, $\psi = \frac{1}{2} \operatorname{asin} \frac{V}{\sqrt{Q^2 + U^2 + V^2}}$
par20	$n_{\text{threads}}$		1 – 100	number of computation threads

**Table C2.** Description of the KYNRLPLI parameters par10 – par20.

The model can be used also for computing polarisation in a very simple toy model where all the local line polarisation in the disc is fully polarised perpendicularly to the disc.

Due to the fact that the non-axisymmetric models integrate the emission over the disc and thus are slower, the model may be run in multiple threads to use all CPU cores available for computing. In this case the XSPEC may need to be run with a preloaded thread library (e.g. `LD_PRELOAD=libpthread.so.0 $HEADAS/bin/xspec`)

As usual for spectral line models inside XSPEC, also the KYNRLPLI model is normalised to the unit total photon flux.

The model parameters, their definitions and possible values are summarised in Tab. C1 and C2.